Meng et al. *Zool. Res.* 2025, 46(5): 1093−1107
https://doi.org/10.24272/j.issn.2095-8137.2024.415
https://cstr.cn/32248.14.zr.2024.415

ZR | Zoological Research

Article Open Access

Abnormal zona pellucida and follicular development in *ZP1*-mutant macaques

Wei Meng[1,#], Bao-Zhen Liu[1,#], Dan Huang[2,#], Yu-Tao Fan[1], Cheng-Gang Xiong[1], Ying-Ting Zhang[1], Lei-Lei Zhao[1], Yong-Long Guo[1], Mu-Hua Lai[2], Xin-Yuan Zhao[1], Ya-Qing Li[1], Shi-Kun Zhao[1], Jing-Tao Zeng[1], Chuan-He Liu[3], Ji-Long Liu[1,*], Chen-Hui Ding[2,*], Shi-Hua Yang[1,*]

[1] *College of Veterinary Medicine*, *South China Agricultural University*, *Guangzhou*, *Guangdong* 510642, *China*

[2] *Key Laboratory of Reproductive Medicine of Guangdong Province*, *School of Life Sciences and First Affiliated Hospital*, *Sun Yat-sen University*, *Guangzhou*, *Guangdong* 510275, *China*

[3] *Instrumental Analysis & Research Center*, *South China Agricultural University*, *Guangzhou*, *Guangdong* 510642, *China*

ABSTRACT

Zona pellucida glycoprotein-1 (ZP1) is essential for maintaining oocyte structural integrity and facilitating fertilization. Mutations in *ZP1* are strongly associated with primary infertility disorders such as fertilization failure and empty follicle syndrome; however, the absence of accurate experimental models has hindered mechanistic understanding and obscured the etiological basis of *ZP1*-related infertility. In this study, CRISPR/Cas9-mediated genome editing was employed to generate two *ZP1*-edited cynomolgus macaques (*Macaca fascicularis*), designated #ZP1-1 (male) and #ZP1-2 (female). Following sexual maturation, oocytes retrieved from #ZP1-2 through superovulation exhibited a marked increase in zona pellucida-deficient oocytes and a significant reduction in maturation rates compared to controls. Integrated analyses, including immunofluorescence staining, transmission electron microscopy, transcriptomic profiling of oocytes, and histopathological examination of ovarian tissue, revealed disrupted folliculogenesis and oocyte anomalies consistent with phenotypes observed in human empty follicle syndrome. These findings establish the *ZP1*-knockout cynomolgus macaque as the first non-human primate model of *ZP1*-related infertility, providing a valuable platform for elucidating disease mechanisms and informing the development of targeted interventions for infertility arising from *ZP* gene mutations.

Keywords: *ZP1*; Zona pellucida; Cynomolgus macaques; Infertility

This is an open-access article distributed under the terms of the Creative Commons Attribution Non-Commercial License (http://creativecommons.org/licenses/by-nc/4.0/), which permits unrestricted non-commercial use, distribution, and reproduction in any medium, provided the original work is properly cited.

Copyright ©2025 Editorial Office of Zoological Research, Kunming Institute of Zoology, Chinese Academy of Sciences

INTRODUCTION

The zona pellucida (ZP) is a glycoprotein-rich extracellular matrix that envelops mammalian oocytes and plays a crucial role in fertilization (Jimenez-Movilla & Dean, 2011; Matzuk et al., 2002). In humans, the ZP is composed of four glycoproteins (ZP1–4) that function in oocyte recognition, binding, and activation (Lefièvre et al., 2004; Liu et al., 2017).

Over the past 25 years, the prevalence of female infertility has markedly increased, affecting approximately 10% of married women globally, with nearly half of these cases attributable to genetic factors (Wassarman & Litscher, 2021). A growing body of evidence implicates abnormalities in ZP proteins in the pathogenesis of infertility (Cao et al., 2024; Hou et al., 2022; Liu et al., 2023; Wei et al., 2022; Zhang et al., 2021). Notably, mutation frequencies in *ZP1* and *ZP3* are elevated in women experiencing repeated *in vitro* fertilization failure relative to fertile controls (Männikkö et al., 2005).

Among ZP genes, *ZP1* has emerged as a critical determinant of matrix assembly and oocyte viability. Loss-of-function mutations in *ZP1* can result in incomplete or dysfunctional ZP formation, leading to failed fertilization (Wassarman & Litscher, 2021). A seminal study by Huang et al. (2014) identified a homozygous frameshift mutation in *ZP1* in a consanguineous family with autosomal recessive inheritance, resulting in oocytes entirely lacking the ZP. Subsequent research by Zhang et al. (2018) reported compound heterozygous *ZP1* mutations leading to primary infertility characterized by ZP-deficient oocytes. Additionally, *ZP1* mutations have been implicated in empty follicle syndrome (EFS), a condition marked by infertility and failed

Received: 22 February 2025; Accepted: 01 September 2025; Online: 03 September 2025

Foundation items: This work was supported by the National Key R&D Program of China (2018YFA0801404, 2023YFC3403400), National Natural Science Foundation of China (81941006), Guangdong Special Support Program (2019BT02Y276), and Specific University Discipline Construction Project (2023B10564003), Guangdong Natural Science Funds for Distinguished Young Scholars (2021B1515020079)

[#]Authors contributed equally to this work

*Corresponding authors, E-mail: jilongliu@scau.edu.cn; dchenh@mail.sysu.edu.cn; yangsh@scau.edu.cn

ovarian stimulation. For example, a patient harboring the c.1169_1176delTTTTCCCA frameshift mutation in *ZP1* produced only two oocytes after superovulation, one with an empty zona and one entirely devoid of the matrix, significantly impairing ovulation (Zhou et al., 2019). Additional homozygous variants (c.1708G>A, p.Val570Met; c.1228C>T, p.Arg410Trp; c.507del, p.His170Ilefs*52) have similarly been associated with EFS and aberrant oocyte morphology (Yuan et al., 2019). Collectively, these findings suggest that *ZP1* mutations can lead to a spectrum of structural defects in the ZP, including thinning, complete absence, and formation of empty or vacuous matrices, accompanied by progressive oocyte degeneration. To date, however, the pathogenic mechanisms driving these abnormalities remain unclear (Dai et al., 2019; Sun et al., 2019; Yuan et al., 2019; Zhou et al., 2019).

Investigations using homozygous *ZP1*-knockout female mice have shown that oocytes were still capable of ZP formation despite complete loss of *ZP1*. The number of oocytes obtained following superovulation was comparable to wild-type controls; however, both fertilization and embryonic development rates were significantly reduced (Rankin et al., 1999). Notably, this phenotype diverges from that observed in humans with *ZP1* mutations, where oocytes often lack a ZP entirely. This discrepancy is likely attributable to species-specific differences in ZP composition. While the human ZP is composed of four glycoproteins (ZP1–4), the mouse ZP consists only of ZP1, ZP2, and ZP3. These structural and functional differences may underlie divergent functional roles of the ZP among species (El-Mestrah et al., 2002; Epifano et al., 1995).

Cynomolgus macaques (*Macaca fascicularis*) exhibit close reproductive homology with humans, including a menstrual cycle averaging approximately 28 days, spontaneous menstruation, a uniparous reproductive pattern, and a similar uterine morphology. Importantly, their ZP composition closely resembles that of humans, comprising ZP1, ZP2, ZP3, and ZP4. These features position the cynomolgus macaque as an ideal non-human primate model for studying human infertility. In the present study, *ZP1*-mutant cynomolgus macaques were generated using CRISPR/Cas9 technology to investigate structural and functional consequences of *ZP1* loss on oocyte quality and folliculogenesis. This study explored the pathogenic mechanisms underlying *ZP1* mutation-related infertility by establishing an animal model that closely mirrors human *ZP1* dysfunction.

MATERIALS AND METHODS

Animals

All cynomolgus macaques used in this study were sourced from Guangdong Blue Island Biotechnology Co. Ltd. (GBIB, China), an accredited member of the Association for Assessment and Accreditation of Laboratory Animal Care. Sexually mature females (age 4–8 years, body weight 3.5–5.0 kg) and males (age 7–8 years, body weight 9.5–11.0 kg) were selected as oocyte and sperm donors, respectively. Additional females aged 4–6 years served as controls for superovulation experiments and were also selected as embryo transfer recipients. All animal procedures, including semen collection, ovarian stimulation, oocyte recovery, abdominal ultrasonography, embryo transfer, cesarean section, and unilateral oophorectomy, were carried out in accordance with the Guide for the Care and Use of Laboratory Animals and were approved by the Institutional Animal Care and Use Committee of GBIB (No. LD2017-003 for generation of *ZP1*-edited macaques) and South China Agricultural University (No. 2024e022 for unilateral oophorectomy).

Gene editing vector preparation and zygote microinjection

The PX459 plasmids (Addgene. #48139, USA) were obtained from Addgene and used as templates for polymerase chain reaction (PCR) amplification. A T7 promoter sequence was added to the Cas9 and single-guide RNA (sgRNA) templates via PCR (Supplementary Table S1). The resulting T7-Cas9 PCR product was gel-purified and subjected to *in vitro* transcription using a mMESSAGE mMACHINE T7 ULTRA Kit (Life Technologies, Cat. No. AM1345, USA). The T7-sgRNA PCR product was similarly purified and transcribed *in vitro* using a MEGAshortscript T7 Transcription Kit (Life Technologies, Cat. No. AM1354, USA). Both Cas9 mRNA and sgRNAs were subsequently purified using a MEGAclear Kit (Life Technologies, Cat. No. AM1908, USA).

Microinjection procedures were performed following previously established protocols (Ma et al., 2016; Zhang et al., 2020). Zygotes were generated using semen collected from male cynomolgus macaques via penile probe electroejaculation. Six female macaques at the onset of menses were administered intramuscular injections of recombinant human follitropin alfa (rhFSH; GONAL-F, Merck Serono, Germany) at a dose of 1.4 μg twice daily for eight consecutive days, followed by 80 μg of recombinant human chorionic gonadotropin alfa (rhCG; OVIDREL, Merck Serono, Germany) on day 9. Cumulus-oocyte complexes were collected by laparoscopic follicular aspiration 33–36 h following rhCG administration. Cumulus cells were removed by pipetting after brief exposure (<1 min) to hyaluronidase (0.5 mg/mL) at 37℃. Metaphase II (MII) oocytes, identified by the presence of a first polar body, were cultured in CMRL-1066 medium supplemented with 0.1% Na-lactate and 10% fetal bovine serum (FBS; HyClone Laboratories, SH30088.02, USA), and fertilized via intracytoplasmic sperm injection (ICSI). At 10–12 h post-ICSI, a mixture containing Cas9 mRNA (100 ng/μL) and sgRNA (50 ng/μL) was injected into the cytoplasm of zygotes using the FemtoJet 4i microinjection system (Eppendorf, Germany). The zygotes were then cultured under mineral oil in hamster embryo culture medium-9 containing 10% FBS at 37℃ in 5% CO_2, 5% O_2, and 90% N_2. Zygotes were cultured for more than 3 days before being collected for genotyping or embryo transfer. Three surrogate mothers were selected based on specific criteria: two consecutive normal menstrual cycles (26–32 days), the presence of a freshly ovulated follicle, and ultrasonographic evidence of a normal uterine cavity. Five eight-cell stage embryos were transferred into one oviduct of each recipient via laparoscopy using a fixed polyethylene catheter. Pregnancy was confirmed by transabdominal ultrasonography upon detection of a conceptus with a beating heart at 25 days post-transfer.

Genotyping and sequencing

Genomic DNA from individual embryos was amplified using a REPLI-g Single Cell Kit (QIAGEN, Cat. No. 150345, Germany). PCR amplification was performed using PrimeSTAR GXL DNA Polymerase (Takara, Cat. No. R050A, Japan). Blood was drawn from mutant monkeys, and tissue DNA was extracted using a Tiangen DP304 kit (China). The

genotyping primers are shown in Supplementary Table S1. The PCR amplicons were gel-purified and sequenced, including Sanger sequencing, plaque clone sequencing, amplicon sequencing, and HiFi sequencing.

For plaque clone sequencing, PCR products were subcloned using a Mighty TA-cloning Reagent Set for PrimeSTAR (Takara, Cat. No. 6019, Japan) and transformed into *E. coli*. The plasmids were purified and analyzed by Sanger sequencing.

Off-target analysis

Potential off-target effects were evaluated by inputting sgRNA sequences into three independent platforms: CRISPOR, Benchling, and Cas-OFFinder. The *Macaca fascicularis* reference genome (9541) was selected for analysis. Predicted off-target sites were compiled across platforms and filtered for consensus regions. Candidate off-target sites were validated by amplifying the corresponding genomic regions using PCR, followed by Sanger sequencing of the PCR products.

Transmission electron microscopy (TEM)

Ultrastructural analysis of oocytes was performed using TEM. Oocytes were fixed in a mixed solution of 2.5% glutaraldehyde and 2% paraformaldehyde at 4°C to preserve cellular integrity. Samples were embedded in agarose to maintain structural stability. Post-fixation was carried out with osmium tetroxide, followed by uranyl acetate staining. Oocytes were then dehydrated with graded ethanol, transitioned to acetone as a solvent, and embedded in epoxy resin. After polymerization, ultra-thin sections (60–90 nm) were prepared using an ultramicrotome, stained with uranyl acetate and lead citrate, and imaged using TEM to visualize subcellular structures and ZP architecture. Five samples were fixed each time. In total, 20 sections were prepared from wild-type (WT) oocytes and 10 sections were prepared from #ZP1-2 oocytes.

Definition and calculation of relative density in TEM images

TEM images were analyzed to quantify the relative gray density of distinct regions within the ZP. Image J software was used for image analysis according to previously established protocols. The following measurement parameters were defined:

Inner region gray value (I_{IN}): Mean gray intensity within the inner ZP, measured within the designated orange box.

Outer region gray value (I_{OUT}): Mean gray intensity within the outer ZP, measured within the designated blue box.

Fibrous structure gray value (I_{CF}): Mean gray intensity of the cross-linked fibrillar structures within the ZP, measured within the designated yellow box.

Background gray value (I_B): Mean gray intensity of the background area devoid of structural components.

Relative density for each region was calculated using the following formulas:

$$\text{Inner region relative density (IN)} = (I_{IN} - I_B)/I_B \quad (1)$$

$$\text{Outer region relative density (OUT)} = (I_{OUT} - I_B)/I_B \quad (2)$$

$$\text{Cross-linked fibrils relative density (CF)} = (I_{CF} - I_B)/I_B \quad (3)$$

Statistical comparisons of the relative densities between #ZP1-2 and #WT oocytes were performed using a two-tailed unpaired Student's *t*-test. This approach enabled quantitative assessment of structural differences in ZP ultrastructure between mutant and control groups.

Hematoxylin and eosin (H&E) staining

Ovarian tissues were fixed in 4% paraformaldehyde at 4℃ for 48 h. Samples were dehydrated in graded ethanol solutions (70% for 6 h, 80% for 1 h, 96% for 1 h, and 100% for 3 h), cleared in xylene, and embedded in paraffin. Sections were cut at a thickness of 5 μm, stained with H&E, and imaged using an inversion microscope.

Single-cell cDNA amplification and single-cell mRNA sequencing

Single-cell cDNA amplification and mRNA sequencing were conducted at BGI (China) using SMART-Seq II amplification (Picelli et al., 2014; Xue et al., 2013). A total of 20 oocytes were collected and stored in BGI-provided cell lysis buffer, then transported on dry ice. Cell lysis was performed on a thermal cycler, followed by first-strand cDNA synthesis using SMART-Seq II amplification.

Subsequently, cDNA was pre-amplified and subjected to quality control (QC) assessments, including concentration measurement, purity evaluation, and gel electrophoresis.After QC, three germinal vesicle (GV)-stage oocytes from #ZP1-2 and three GV-stage WT oocytes were returned for downstream validation.The quantitative PCR primers are shown in Supplementary Table S2.The remaining samples, including four #ZP1-2 GV, two #ZP1-2 MII, three WT GV, and five WT MII oocytes, were used for library construction and high-throughput sequencing.

RNA sequencing (RNA-seq) analysis

Clean reads were aligned to the *Macaca fascicularis* reference genome (mfa5.0) using TopHat2 (Kim et al., 2013), with annotations provided in GFF format. Transcript assembly and quantification were performed using featureCounts (Liao et al., 2014) to generate gene-level counts from BAM alignment files. Differential expression analysis was conducted using DESeq2 (Love et al., 2014), with normalization and estimation of differentially expressed genes (DEGs). To improve fold-change (FC) reliability and mitigate the influence of outliers, the "apeglm" shrinkage method was applied to stabilize effect size estimates for low-count genes (Zhu et al., 2019).

Functional enrichment analysis of DEGs—including Kyoto Encyclopedia of Genes and Genomes (KEGG) pathway enrichment, Gene Ontology (GO) annotation, and gene set enrichment analysis (GSEA)—was performed using ClusterProfiler v.4.0 (Wu et al., 2021). All sequencing data and analysis code have been deposited in the public database [10.57760/sciencedb.j00139.00211] for further research use.

ZP dissection and cytoplasm isolation

Under an inverted microscope, individual oocytes were stabilized using a holding pipette to orient the ZP for precise manipulation. A microneedle was inverted into the perivitelline space to puncture the ZP. The needle was gently rubbed against the holding pipette to create an initial rupture. A cross-shaped incision was then made at the perforation site to generate an appropriately sized opening.

After creating the incision, the injection needle was replaced with a biopsy needle, which was positioned at the ZP opening. Gentle suction was applied to extract the cytoplasm while maintaining the integrity of the oocyte membrane and other structures. The procedure was conducted under sterile conditions at 37°C to preserve oocyte viability. The size of the

ZP incision was carefully controlled to allow efficient cytoplasmic extraction without compromising the overall integrity of the oocyte. This technique enabled precise isolation of the cytoplasm for downstream analysis.

Protein extraction and mass spectrometry analysis

Samples were collected from #ZP1-2 GV, WT GV, #ZP1-2 MII, WT MII, #ZP1-2 ZP, WT ZP, #ZP1-2 cytoplasm, and WT cytoplasm using a micromanipulation system. Each group comprised three pooled oocytes, except for ZP samples, which included six pooled oocytes per group to meet protein loading requirements. All samples were transported on dry ice to the Zhongke New Life Technology Center (China).

At the facility, samples underwent in-solution enzymatic digestion using SP3 magnetic bead-based sample preparation (Müller et al., 2020). Proteins were extracted using SDT lysis buffer supplemented with protease inhibitors and processed for data-independent acquisition (DIA) mass spectrometry. Each sample was subjected to one round of DIA-based proteomic profiling.

For DIA analysis, chromatographic separation was performed using the Nanoelute system under nanoscale flow rates. The separated samples were analyzed on a timsTOF mass spectrometer (Bruker) under a DIA strategy.

Protein data preprocessing

DIA data were analyzed using Spectronaut software (China), referencing the same database used for spectral library construction. If spectral libraries were unavailable, the direct DIA approach was employed for peptide identification.

Key software parameters were set as follows: Retention time prediction type: dynamic iR, Interference correction at the MS2 level: enabled, Cross-run normalization: enabled, *Q*-value cutoff=0.01 (false discovery rate (FDR)<1%). All identified proteins and peptides were filtered using these parameters to ensure high-confidence quantification.

GO functional annotation and KEGG pathway enrichment of proteins

GO annotation of the target protein set was performed using Blast2GO. KEGG pathway annotation was conducted using the KEGG Automatic Annotation Server (Shanghai, China). Enrichment analyses for GO categories, KEGG pathways, and protein domains were carried out by comparing their distributions between the target and background protein sets using Fisher's exact test. All bioinformatic analyses were conducted using the Zhongke APT-BioCloud platform (China).

Oocyte immunofluorescence staining

Immunofluorescence staining was performed to analyze the localization and expression of ZP proteins (ZP1, ZP2, ZP3, and ZP4) within oocytes. To preserve cellular and protein structures, oocytes were fixed in formaldehyde for 30 min, followed by multiple washes with phosphate-buffered saline (PBS) to remove residual fixative. Nonspecific antibody binding was minimized by incubating samples in blocking solution at 37°C for 1 h.

Primary antibodies targeting ZP1 (Invitrogen, PA5-101973, USA), ZP2 (Invitrogen, PA5-87653, USA), ZP3 (Invitrogen, PA5-89033, USA), and ZP4 (Invitrogen, PA5-101973, USA) were diluted 1:200 and incubated with oocytes at 4°C overnight to ensure specific binding. After thoroughly washing with PBS to remove unbound primary antibodies, fluorophore-conjugated secondary antibodies were applied at a dilution of 1:600 and incubated at room temperature in the dark for 30 min to protect against photobleaching. Excess secondary antibodies were removed through additional PBS washes.

For nuclear staining, oocytes were incubated with 4',6-diamidino-2-phenylindole (DAPI) for 10 min at room temperature, followed by a final series of PBS washes to eliminate any unbound dye. High-resolution imaging was performed using a confocal laser scanning microscope (CLSM), allowing for detailed observation of the distribution and organization of proteins within the ZP. This approach facilitated detailed assessment of structural and functional changes associated with ZP protein expression.

Laparoscopic oophorectomy

Laparoscopic surgery was performed to excise ovarian tissue with high precision while minimizing surgical trauma. Following general anesthesia and limb restraint, a small incision was made lateral to the umbilicus to provide access for the laparoscopic instruments. Carbon dioxide was insufflated into the abdominal cavity to establish pneumoperitoneum, creating a clear operative field. A laparoscope connected to an imaging system was inserted through the trocar, enabling real-time observation of the abdominal cavity.

Two additional small incisions were made adjacent to the primary entry site to accommodate laparoscopic instruments such as forceps and scissors. Under continuous visual guidance, the ovary was carefully dissected and separated from surrounding structures. Ovarian blood vessels were ligated to prevent bleeding, and the ovary was completely excised and retrieved through the trocar port for subsequent analysis. After the ovary was removed, the surgical site was inspected for any residual bleeding, and the abdominal cavity was thoroughly irrigated with sterile saline. Pneumoperitoneum was released, the trocar was removed, and all incisions were sutured or sealed. Postoperative care included intramuscular administration of penicillin (25 mg/kg body weight) to prevent infection and meloxicam (0.4 mg/kg body weight) for analgesia. This laparoscopic approach ensured effective ovary removal while preserving tissue integrity for subsequent experimental procedures.

Protein structure prediction and template modeling score analysis

Mutant ZP1 protein structures were predicted using the AlphaFold3 web-based platform, a state-of-the-art system for protein folding prediction based on advanced deep learning algorithms (Abramson et al., 2024). Full-length amino acid sequences of the target proteins were submitted to the AlphaFold3 server (https://golgi.sandbox.google.com/) to generate three-dimensional structural models. Predictions were performed using default parameters to ensure consistency. The resulting protein structures were downloaded and prepared for subsequent analysis.

To evaluate structural similarity between predicted mutant models and corresponding reference structures, template modeling scores (TM-Scores) were calculated using the TM-Score web server (Zhang & Skolnick, 2005). Structural alignments were performed by uploading predicted and reference protein models to the TM-Score platform (https://zhanggroup.org/TM-score/). TM-Scores were used as a quantitative measure of structural similarity, with values above 0.5 indicating significant structural similarity and values below 0.5 suggesting limited structural alignment.

Statistical analysis

All quantitative data are expressed as mean±standard error of the mean (SEM), based on a minimum of three independent replicates. Statistical significance was determined using Student's *t*-test implemented in R. A *P*-value of less than 0.05 was considered statistically significant, with significance levels denoted as follows: *: $P<0.05$; **: $P<0.01$; ***: $P<0.001$.

RESULTS

Generation of *ZP1*-mutant cynomolgus macaques via CRISPR/Cas9

To investigate the impact of ZP1 on oocyte development, *ZP1* gene-edited cynomolgus macaques were generated. Four sgRNAs targeting exons 5, 8, and 10 of the *ZP1* gene were designed (Figure 1A). Embryo testing revealed that sgRNA1 and sgRNA2 were inactive, while sgRNA3 and sgRNA4 displayed 100% and 70% editing activity, respectively (Figure 1B). A mixture containing sgRNA3, sgRNA4, and Cas9 mRNA was microinjected into pronuclear-stage embryos. Fifteen embryos were transferred into the oviducts of three surrogate macaques via laparoscopy. One surrogate, M3, successfully delivered live-born twins (Figure 1C), designated as #ZP1-1 (male) and #ZP1-2 (female).

Amplicon and long-read sequencing of peripheral blood samples revealed that #ZP1-1 carried three distinct genotypes: a 49 bp deletion (60%), an Ins3bp-Del9bp (26%), and an Ins2bp-Del54bp (14%) (Figure 1D; Supplementary Figure S1A). Sequencing of #ZP1-2 revealed a 463 bp deletion in exon 11 near regions of *ZP1* (Figure 1F; Supplementary Figure S1B). Final genotyping identified four allelic variants in #ZP1-2: Del4bp (32%), Ins2bp-Del5bp (29%), Del23bp (18%), and Del463bp (21%) (Figure 1E; Supplementary Figure S1A).

To assess the structural consequences of these mutations, AlphaFold3 was used to predict the structures of the WT ZP1 protein and its four mutant isoforms. TM-Scores were evaluated to assess structural similarities. Among the mutants, Mut1 exhibited the highest overall similarity to the WT protein (TM>0.5) (Supplementary Figure S1C, D), suggesting a relatively mild phenotype for #ZP1-2 oocytes. All AlphaFold3 predictions have been deposited in the public database (10.57760/sciencedb.j00139.00211).

Off-target effects associated with sgRNA3 and sgRNA4 were systematically evaluated using three widely used prediction tools: Cas-OFFinder, Benchling, and CRISPOR. The intersection of predicted off-target sites from all three platforms identified 23 potential candidate sites for *ZP1*-sgRNA3 and 20 for *ZP1*-sgRNA4 (Figure 1G; Supplementary Figure S2A, B). Amplicon sequencing confirmed three off-target sites (Supplementary Figure S2C–F). Two off-target sites were located in intergenic regions, while one site was detected within an intronic region of the *TBC1D14* gene. Quantitative PCR analysis revealed no significant difference in *TBC1D14* expression between mutant and WT macaques (Supplementary Figure S2G).

Collectively, these results confirm the successful generation of *ZP1*-edited cynomolgus macaques, providing a primate model for investigating ZP1-associated reproductive dysfunction.

Abnormal ZP structure in *ZP1*-mutant cynomolgus macaque oocytes

To assess the effects of *ZP1* knockout on ZP architecture and oocyte quality, three rounds of superovulation were performed on the sexually mature female #ZP1-2 macaque at 4 years of age, with each induction spaced more than three months apart. For comparison, seven age-matched WT females (#WT) were also superovulated, and their oocytes were collected. Analysis revealed a markedly higher proportion of oocytes from #ZP1-2 exhibiting empty or structurally incomplete ZP compared with controls (Supplementary Figure S3A). Even oocytes appearing macroscopically intact in #ZP1-2 frequently displayed uneven ZP thickness (Figure 2A). The overall incidence of oocyte abnormalities, including those with empty ZP, cytoplasmic compaction, or degeneration, was significantly higher in #ZP1-2 than in #WT (Figure 2B; Supplementary Figure S3B; Supplementary Table S3), mirroring clinical phenotypes reported in human ZP1 mutation cases and consistent with features of EFS (Yuan et al., 2019).

The ZP can be divided into inner and outer regions based on sperm-binding properties (Moros-Nicolás et al., 2021), which are associated with distinct fibrillar architectures: the outer region contains loosely organized, net-like filaments, while the inner region is composed of densely packed fibers aligned perpendicularly to the oolemma (Familiari et al., 2006; Phillips & Shalgi, 1980). To investigate structural differences at the ultrastructural level, TEM was performed on five GV-stage oocytes from both #ZP1-2 and #WT macaques (Figure 2C; Supplementary Figure S3A). While overall ZP thickness in the inner and outer regions did not differ significantly between groups (Figure 2D), #ZP1-2 oocytes exhibited irregular and inconsistent regional thicknesses (Supplementary Figure S4B, C). TEM analysis revealed distinct ultrastructural defects in #ZP1-2 oocytes. Compared to the well-defined inner and outer layers of the ZP in #WT oocytes—characterized by dense inner fibrils and sharply delineated boundaries—the ZP in #ZP1-2 oocytes appeared poorly organized, with indistinct boundaries between regions, reduced fibrillar density, and a lack of high-electron-density granules in the outer layer (Figure 2E; Supplementary Figure S4A).Quantitative optical density analysis indicated significantly reduced ZP density in #ZP1-2 compared to #WT (Figure 2F). Notably, two oocytes from #ZP1-2 exhibited the lowest measured ZP densities, with no discernible boundary between the inner and outer regions (Supplementary Figure S5A, B). These findings demonstrate substantial ZP disorganization and compromised ultrastructural integrity in oocytes from ZP1-mutant macaques.

Reduced RNA and protein expression of specific ZP components in #ZP1-2 oocytes

To determine whether ZP1 gene mutations affect the expression of ZP glycoproteins, MII- and GV-stage oocytes were collected from #ZP1-2 and #WT macaques for single-oocyte RNA-seq (Supplementary Figure S7A; Figure 3A). Enrichment analysis of the top 200 up-regulated and down-regulated genes in the GV-stage group revealed expression trends that were largely conserved in the MII-stage oocytes, suggesting that the most significant differential pathways may persist across these developmental stages. Notably, *ZP1* expression was significantly reduced in #ZP1-2 oocytes (Figure 3B; Supplementary Table S4). To validate this transcriptional down-regulation, reverse transcription primers targeting exons 9 and 11 of the *ZP1* gene were designed (Figure 3C). Quantitative PCR analysis confirmed that *ZP1* mRNA levels in #ZP1-2 oocytes were reduced to approximately one-third of those in #WT oocytes (Figure 3D),

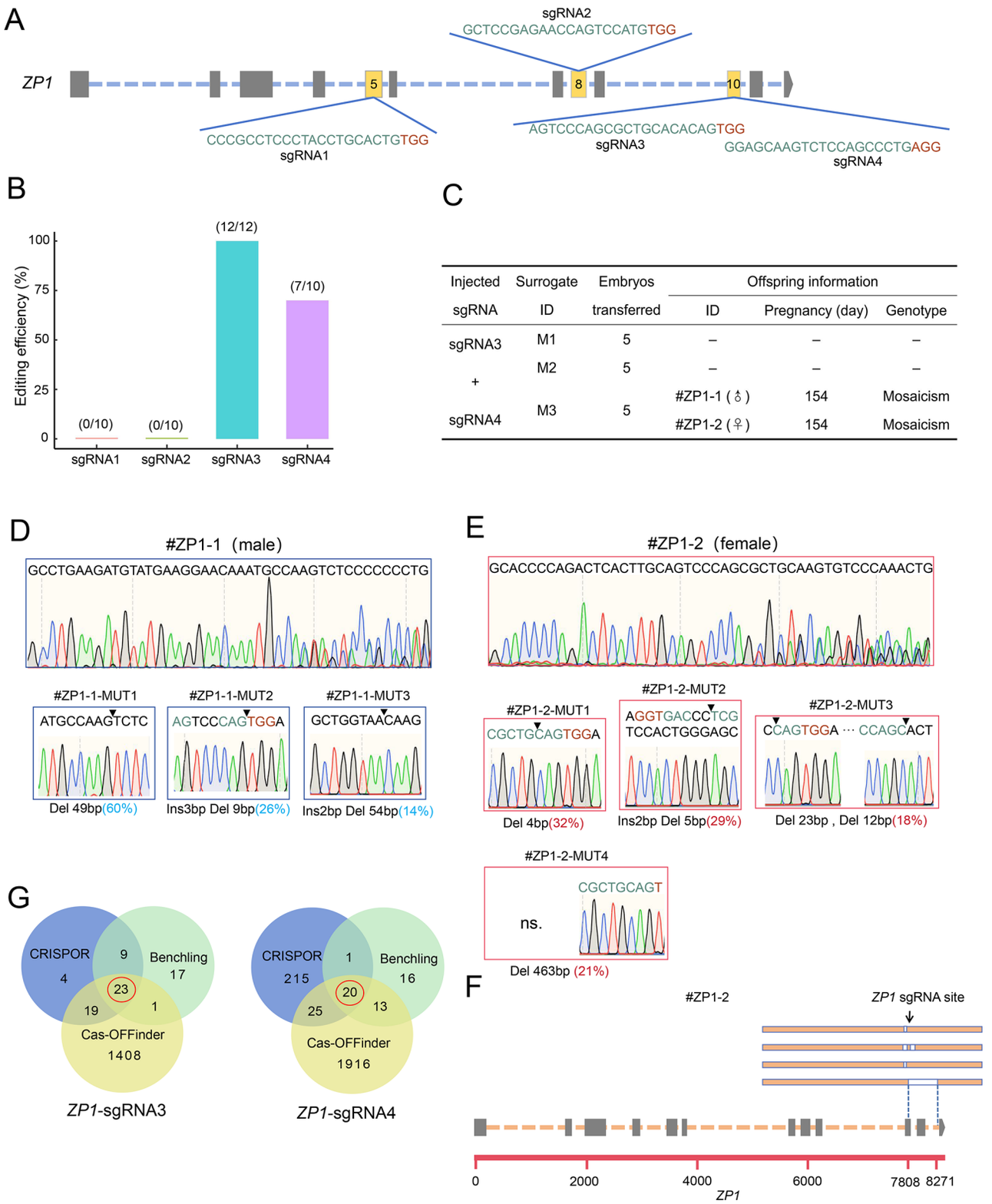

Injected sgRNA	Surrogate ID	Embryos transferred	Offspring information		
			ID	Pregnancy (day)	Genotype
sgRNA3	M1	5	–	–	–
+	M2	5	–	–	–
sgRNA4	M3	5	#ZP1-1 (♂)	154	Mosaicism
			#ZP1-2 (♀)	154	Mosaicism

Figure 1 Generation of *ZP1*-edited cynomolgus macaques

A: Schematic of *ZP1* gene and sgRNA target sites. Green regions represent sgRNA sequences; red regions indicate protospacer adjacent motifs (PAMs). B: Editing efficiencies of individual sgRNAs in embryo testing. C: Summary of transferred *ZP1*-edited embryos and resulting offspring, –: Not available. D, E: Genotypic characterization of #ZP1-1 and #ZP1-2, with editing frequencies shown in brackets. Red bases represent PAMs; green represents sgRNA sequences. F: HiFi sequencing results of peripheral blood from #ZP1-2. G: Intersection of potential off-target sites identified using Cas-OFFinder, CRISPOR, and Benchling platforms.

with similar down-regulation trends observed for *ZP3* and *ZP4* (Figure 3E). These results indicate that *ZP1* mutation may influence the transcriptional regulation of *ZP3* and *ZP4*.

To further characterize transcriptional disruptions at the MII stage, pathway enrichment analysis was performed on DEGs (Supplementary Figure S6A, B). KEGG pathway analysis

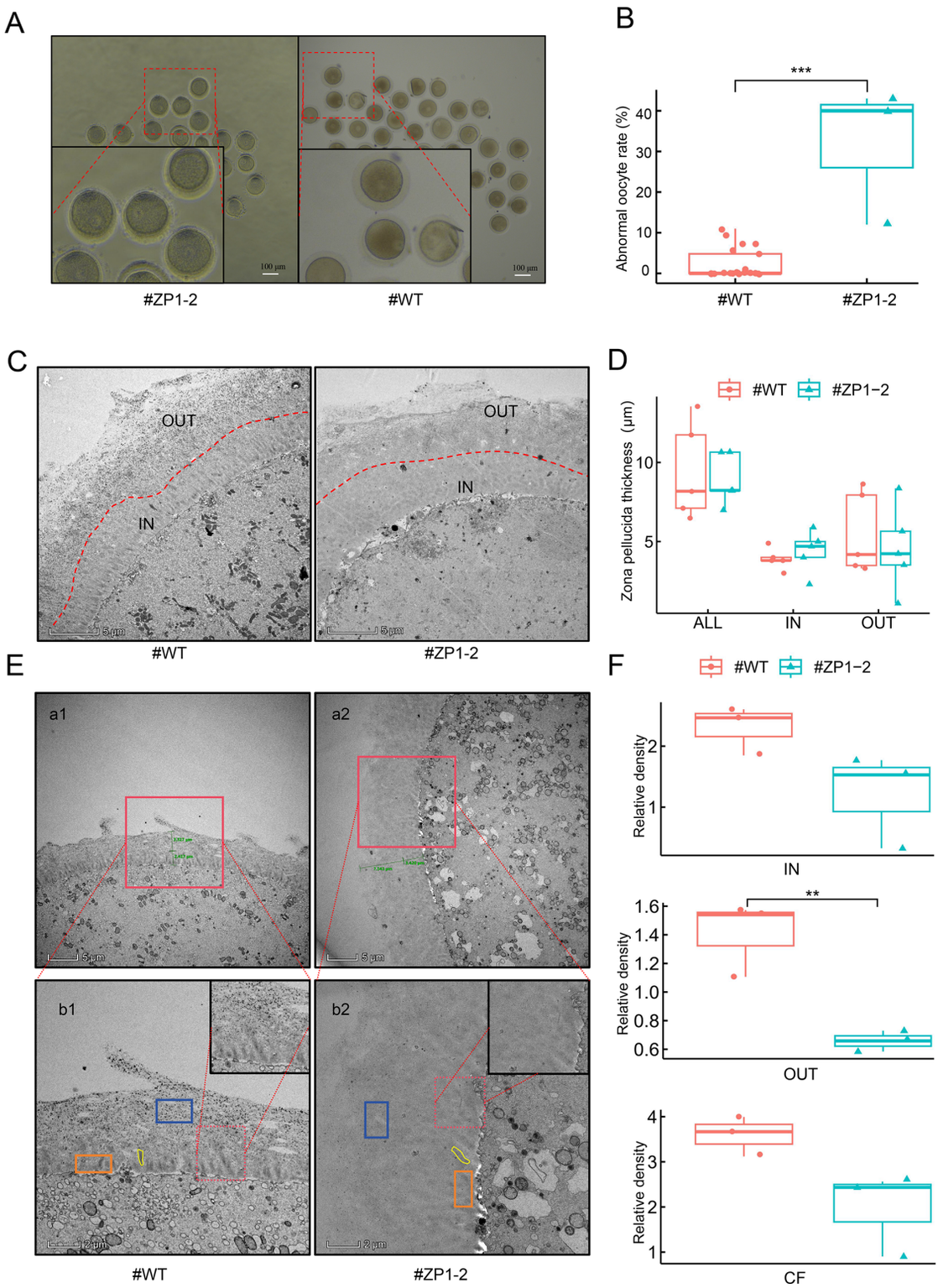

Figure 2 *ZP1*-mutant cynomolgus macaques exhibit abnormal zona pellucida (ZP)

A: Bright field images of oocyte ZP from #ZP1-2 and #WT macaques. Scale bar: 100 μm. Red circles highlight oocytes from #ZP1-2 with irregular ZP thickness. B: Comparison of abnormal oocytes relative to total oocytes retrieved over three superovulation cycles in #ZP1-2 and #WT groups. Student's *t*-test, **: $P<0.01$. C: Transmission electron microscopy (TEM) ultrastructure images of GV-stage oocyte ZP from #ZP1-2 and #WT macaques. Inner (IN) and outer (OUT) ZP regions are demarcated by a red line. Scale bar: 5 μm. D: Comparison of total (ALL), inner (IN), and outer (OUT) ZP thickness in GV-stage oocytes from #ZP1-2 and #WT macaques (n=5 oocytes per group). E: a1 and a2: TEM images of #WT and #ZP1-2 oocytes. Scale bar: 5 μm. b1 and b2 are magnified views of a1 and a2, respectively. Scale bar: 2 μm. Orange box represents IN region; blue box represents OUT region; yellow area represents fibrous structure. F: Quantitative comparison of TEM density between #ZP1-2 and #WT oocytes. Gray levels were measured using ImageJ, where I_{IN} represents gray value of IN region (orange box), I_{OUT} represents gray value of OUT region (blue box), I_{CF} represents gray value of cross-linked fibrils (yellow box), and I_B represents average gray value of background. Relative density of the IN region was calculated using the formula: TEM relative density IN=$(I_{IN}-I_B)/I_B$. Statistical analysis performed using Student's *t*-test.

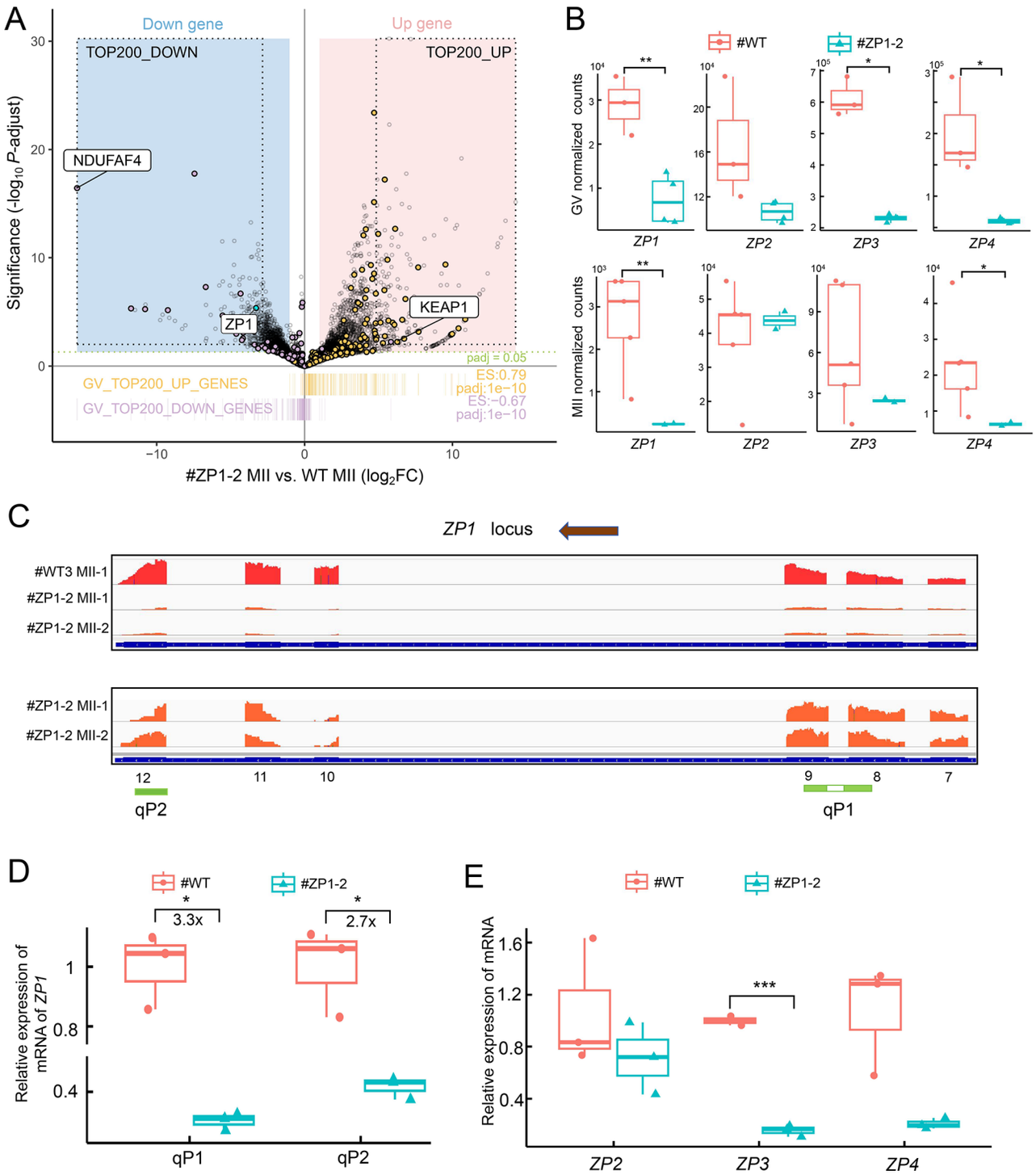

Figure 3 Differential gene expression and regulation of zona pellucida (ZP) genes in *ZP1*-mutant and WT oocytes

A: Volcano plot showing differentially expressed genes (DEGs) in *ZP1*-mutant GV-stage oocytes. X-axis represents log2 fold change; y-axis represents significance level as $-\log_{10}$(*P*-adjust). Genes significantly down-regulated and up-regulated are highlighted in blue and red, respectively. Key genes, such as *NDUFAF4* (down-regulated) and *ZP1* (down-regulated), are labeled. Green dotted line indicates adjusted *P*-value threshold (*P*-adjust=0.05). Enrichment analyses for GV_TOP200_UP_GENES and GV_TOP200_DOWN_GENES are displayed below, with corresponding enrichment scores (ES) and *P*-values. #WT (*n*=5) and #ZP1-2 (*n*=2). B: Boxplots showing normalized expression levels of key DEGs (*P*-adjust<0.05 or *P*-adjust<0.01) in *ZP1*-mutant (blue) and WT (red) oocytes. Each panel represents a specific gene or pathway, with y-axis showing normalized expression levels (log-transformed). Statistical significance thresholds are indicated in the top-left corner of each panel. Dots represent individual data points; horizontal lines within boxes denote median values. C: Visualization of RNA-seq results for *ZP1* in #WT and #ZP1-2 oocytes using Integrative Genomics Viewer (IGV). qP1 and qP2 represent two designed RT product sequences flanking but not including the editing site. D and E: Comparison of mRNA expression levels of ZP genes. Student's *t*-test, *: *P*<0.05; ***: *P*<0.001. Each group *n*=3.

ranked by adjusted *P*-value (*P*-adjust) identified significant down-regulation in mitochondrial-related functions, particularly the tricarboxylic acid (TCA) cycle and oxidative phosphorylation pathways. Subsequent GSEA revealed

additional dysregulated mitochondrial functions, including pathways related to autophagy. Similar findings were observed in the GV-stage enrichment analyses (Supplementary Figure S7C–E). These results suggest that ZP1 mutations may broadly impair mitochondrial function and related metabolic processes in oocytes.

To evaluate the impact of ZP1 deficiency on protein localization and abundance within the ZP, immunofluorescence staining was performed. In #WT oocytes, ZP1 and ZP3 proteins were primarily concentrated in the outer ZP, while ZP2 and ZP4 were predominantly found in the inner region (Figure 4A). In contrast, #ZP1-2 oocytes exhibited a marked reduction in ZP1 protein (Figure 4C) and diminished ZP3 signal intensity (Figure 4D). The levels and distribution of ZP2 and ZP4 remained largely unchanged (Supplementary Figure S8). Line-scan fluorescence analysis across oocytes demonstrated an absence of distinct ZP1 fluorescence peaks in #ZP1-2, indicating near-complete loss of ZP1 in the outer region. In contrast, #WT oocytes displayed strong ZP1 fluorescence bands, highlighting its presence in the outer

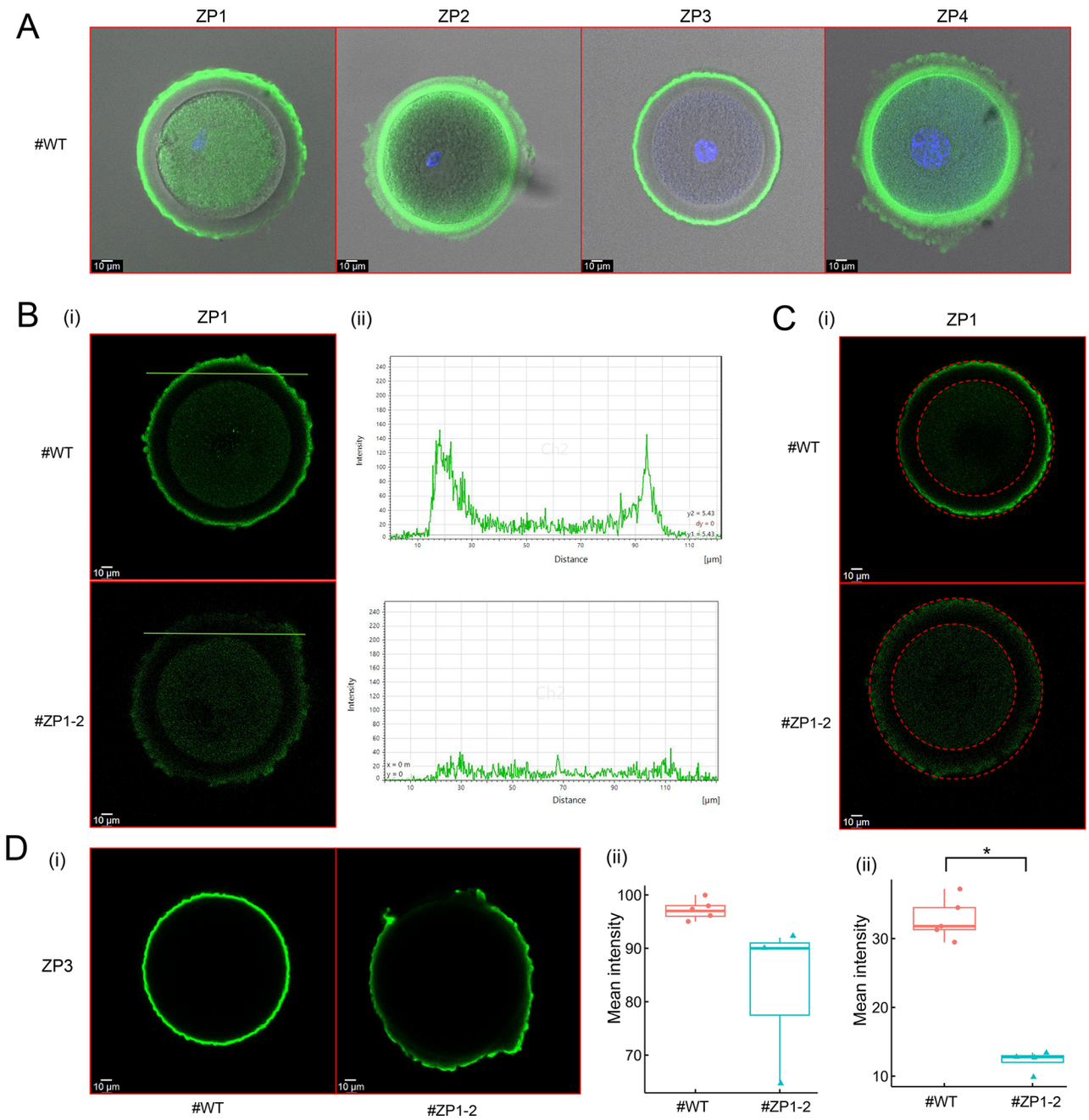

Figure 4 Proteomic and immunofluorescence analyses reveal reduced zona pellucida (ZP) protein levels in ZP1-mutant oocytes

A: Representative localization of ZP proteins in GV-stage oocytes and surrounding ZP from #WT macaques. B: (i) Immunofluorescence staining of ZP1 in the ZP of GV-stage oocytes from #ZP1-2 and #WT macaques. A line ROI was drawn across the ZP to measure fluorescence distribution. (ii) Corresponding fluorescence intensity profiles along the ROI line, indicating reduced ZP1 signal in #ZP1-2. C: Quantification of ZP1 fluorescence intensity in the ZP. (i): Measurement ranges of immunofluorescence of ZP1 intensity in GV-stage oocytes in #ZP1-2 and #WT macaques. (ii) Mean fluorescence intensity of ZP1, with statistical comparison between #ZP1-2 and #WT (n=3, Student's t-test, *: P<0.05). D: (i) Immunofluorescence staining of ZP3 in ZP of #ZP1-2 and #WT oocytes. (ii) Quantification of ZP3 mean fluorescence intensity (n=3, Student's t-test, *: P<0.05).

region (Figure 4B).

ZP1 mutation may affect follicular development and oocyte development potential

Re-superovulation experiments revealed a significantly reduced oocyte maturation rate of #ZP1-2 compared to #WT macaques. Following ICSI, a markedly lower proportion of #ZP1-2 MII-stage oocytes progressed to the blastocyst stage (Figure 5A, B; Supplementary Figure S3B), with embryos showing developmental arrest and cleavage failure, indicating compromised embryonic potential. Transcriptomic analysis of single oocytes showed enrichment of HALLMARK gene sets (Liberzon et al., 2015). In the GV-stage group, the G2M checkpoint pathway was the most significantly enriched (Supplementary Figure S7A), suggesting possible mitotic arrest. Although this pathway did not reach statistical significance in the MII-stage group, an overall up-regulation trend was still evident. In contrast, the most significantly down-regulated KEGG pathway in the MII-stage group was the cell cycle (Supplementary Figure S6B). These findings suggest that disruption of mitotic cycle regulation in ZP1-deficient oocytes may underlie the observed embryonic developmental arrest.

To further investigate the impact of ZP1 mutation on folliculogenesis, unilateral oophorectomy was performed on both #ZP1-2 and #WT macaques for histological analysis. H&E staining revealed structural abnormalities across various follicular stages in #ZP1-2, including primordial, primary/secondary, and antral follicles (Figure 5C, D). Among these, primordial follicles exhibited the most pronounced morphological defects (Figure 5D). Additionally, a clear separation between the ZP and granulosa cells was observed in #ZP1-2 macaques, whereas #WT macaques displayed an intact ZP-granulosa cell interface.

Consistent with these observations, gene sets involved in “ligand-complement activation” and “G-protein coupled receptor activation”, key mediators on granulosa cell-oocyte interactions, were significantly down-regulated in #ZP1-2 oocytes (Supplementary Figure S7B, C). This suggests that ZP1 deficiency disrupts communication between granulosa cells and oocytes, hindering follicle maturation. Additionally, pathways related to endocytosis were up-regulated, potentially reflecting a compensatory mechanism by which oocytes attempt to acquire nutrients in the absence of adequate granulosa cell support.

ZP1 mutation potentially induces oxidative stress leading to oocyte degeneration

To evaluate the effects of ZP1 mutation on oocyte quality, proteomic profiling was performed on GV- and MII-stage oocytes collected from superovulated #ZP1-2 and #WT macaques. In addition, cytoplasm and ZP fractions were isolated using micromanipulation techniques for separate analysis. Initial quality assessment of proteomic data, including total peptide and protein counts, revealed that the #ZP1-2_GV group had significantly fewer peptides and proteins compared to other GV, MII, and cytoplasmic samples (CYT) (Supplementary Figure S9A), suggesting potential sample degradation. Consequently, this group was excluded from downstream analyses. As expected, the ZP samples yielded fewer protein identifications, likely due to the inherently low protein abundance in the ZP. However, the experimental and control groups showed relatively consistent results. Differentially expressed proteins from the MII, CYT, and ZP groups are summarized in Supplementary Figure S9B. As anticipated, ZP1 protein levels were significantly reduced in the #ZP1-2 group, consistent with RNA data (Figure 6A; Supplementary Table S5; Supplementary Table S6). GSEA of the MII-stage proteomic data revealed that the top 20 significantly enriched pathways were predominantly associated with NADPH, ATP, and mitochondrial functions (Figure 6B), indicating that ZP1 mutation exerts a major effect on mitochondrial processes at the protein level.

To further dissect mitochondrial dysfunction, enrichment analysis was conducted on mitochondrial-related GO terms across GV_RNA, MII_RNA, and MII_PRO datasets, including only terms with $P<0.05$ in at least one dataset (Supplementary Table S7). The GV_RNA and MII_RNA groups showed a highly concordant pattern, with mitochondrial transcription and translation pathways consistently down-regulated and mitochondrial autophagy and apoptosis-related pathways consistently up-regulated (Figure 6C). Similar trends were observed in the MII_PRO dataset, with down-regulation in mitochondrial translation and transcription and up-regulation in mitochondrial autophagy and apoptosis. However, discrepancies arose in respiration-related pathways: mitochondrial respiration and energy production were up-regulated at the protein level (MII_PRO) but not reflected at the transcriptomic level (GV_RNA and MII_RNA), suggesting possible post-transcriptional regulation or compensatory protein-level responses.

Although the cytoplasmic fraction only represents a subcellular compartment, analysis of the CYT group also highlighted significant mitochondrial-related pathway enrichment (Supplementary Figure S9C). Key enriched pathways included “mitochondrial respiratory chain complex I” and “inner mitochondrial membrane protein complex”, mirroring the top mitochondrial pathways identified in the MII_PRO group. Furthermore, in the CYT group, mitochondrial RNA processing (GO:0000963 and GO:0000959) was down-regulated, while mitochondrial apoptosis-related pathways were up-regulated. Most mitochondrial respiration-related gene sets were up-regulated, consistent with the patterns observed in the MII_PRO group (Supplementary Table S7).

Collectively, these data suggest that ZP1 deficiency induces oxidative stress and mitochondrial dysregulation, leading to increased autophagy and eventual oocyte degeneration. Supporting this conclusion, TEM analysis further revealed extensive mitochondrial swelling in #ZP1-2 oocytes at both the GV and MII stages (Figure 6E). Most swollen mitochondria lacked cristae, a hallmark of severe mitochondrial injury and a potential indicator of overcompensatory metabolic stress preceding cell death.

Transcriptomic data further revealed significant down-regulation of NDUFAF4 in both groups. This gene, primarily involved in mitochondrial complex I assembly, was almost undetectable in #ZP1-2 oocytes at both GV and MII stages. Conversely, KEAP1, a regulator of oxidative stress responses, was among the top 200 up-regulated genes in #ZP1-2, but almost undetectable in #WT oocytes. KEAP1 promotes the ubiquitination and degradation of NRF2, a transcription factor responsible for up-regulating antioxidant genes such as SOD2 and CAT. As expected, both SOD2 and CAT showed significantly reduced mRNA expression in GV-stage oocytes (Supplementary Figure S9D). In MII-stage oocytes, SOD2 and CAT also exhibited a more than 2-fold reduction in expression at the protein level. Conversely, ALOXE3 and ALOX12B, as

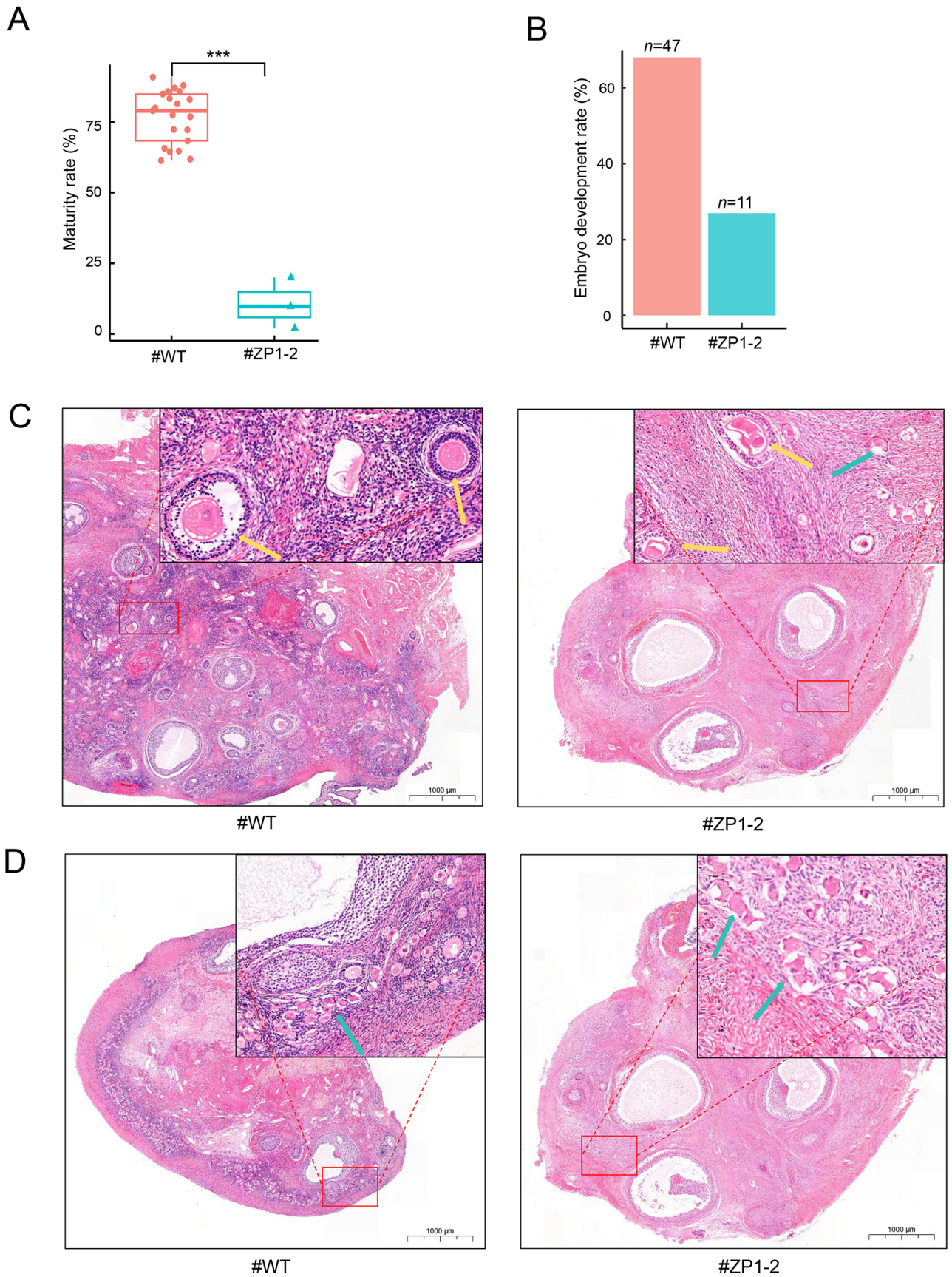

Figure 5 *ZP1* deficiency in #ZP1-2 macaques impairs follicular development and oocyte competence

A: Maturation rates of oocytes retrieved from #WT and #ZP1-2 macaques, defined as the proportion of MII-stage oocytes to total oocytes retrieved. #WT data were collected from three superovulation cycles across seven animals (n=21), while #ZP1-2 data were obtained from three superovulation cycles in a single animal. Statistical comparison was conducted between groups. B: Blastocyst formation rates following ICSI in fertilized oocytes from #ZP1-2 and #WT. C, D: Representative H&E-stained ovarian sections showing growing (B) and primordial follicles (C) from #WT and #ZP1-2 macaques. Yellow arrows indicate growing follicles; blue arrows denote primordial follicles.

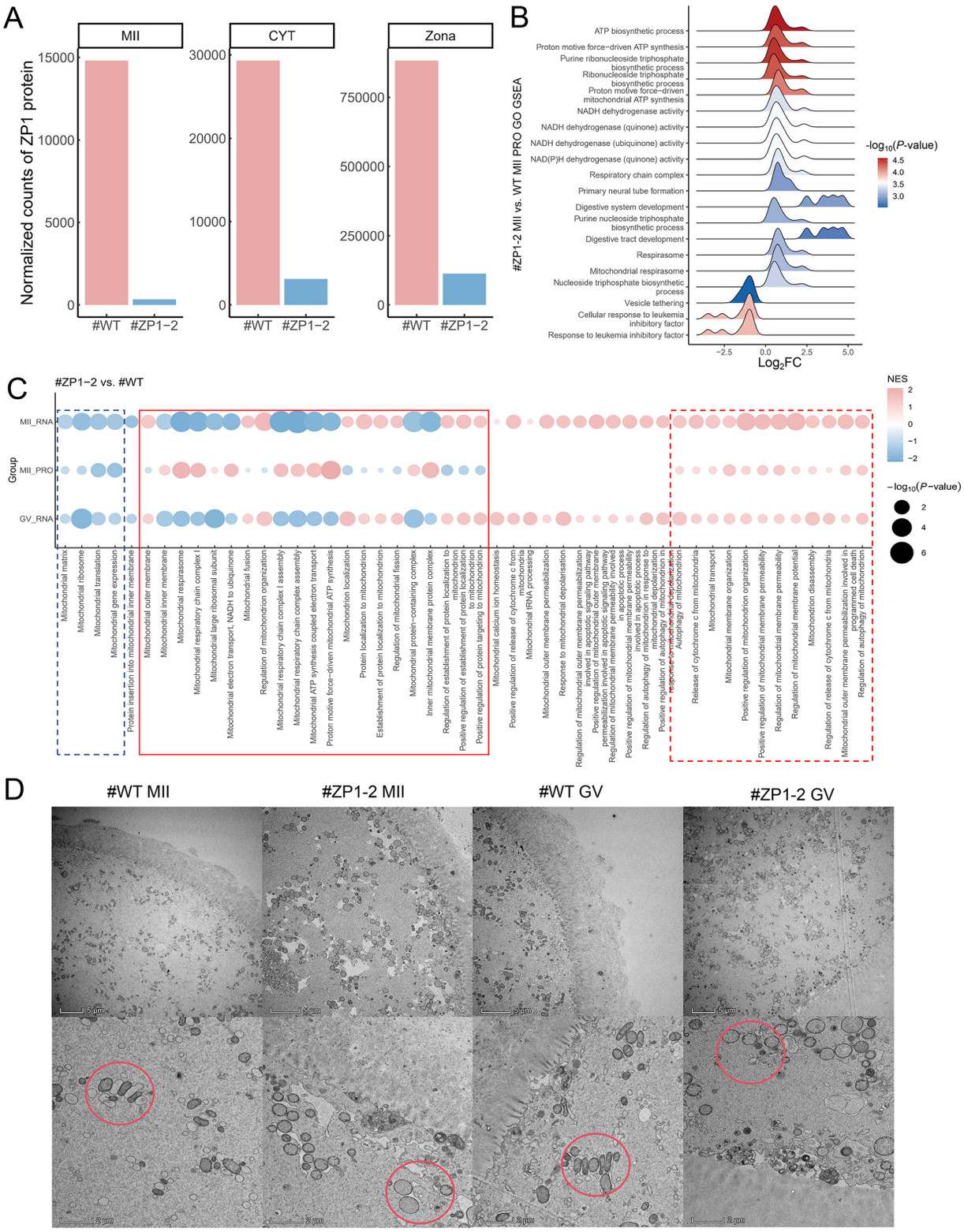

Figure 6 Transcriptomic, proteomic, and ultrastructural evidence of mitochondrial dysfunction in *ZP1*-deficient oocytes

A: Normalized ZP1 protein levels across cytoplasmic (CYT), MII-stage oocyte (MII), and zona pellucida (ZP) fractions in #WT and #ZP1-2 macaques. Protein counts were significantly higher in #WT than in #ZP1-2 across all fractions. B: Gene set enrichment analysis (GSEA) comparing transcriptomic profiles of #ZP1-2 and #WT MII-stage oocytes. C: Enrichment analysis of indicated gene sets across different groups (MII_RNA, MII_PRO, GV_RNA, and GV_PRO). Each row represents a group; each column represents a specific gene set. Color scale represents normalized enrichment score (NES), with red and blue indicating up-regulated and down-regulated pathways, respectively. Size of bubbles corresponds to significance of enrichment, with larger bubbles indicating smaller *P*-values ($-\log_{10}$(*P*-value)). Blue dashed box indicates gene sets commonly down-regulated in both the MII_PRO and MII_RNA groups. Red solid box indicates gene sets with inconsistent regulation between the MII_PRO and MII_RNA groups. Red dashed box indicates gene sets commonly up-regulated in both the MII_PRO and MII_RNA groups. D: Comparison of mitochondrial morphology between #ZP1-2 and #WT under electron microscopy. Red circles indicate mitochondrial swelling.

well as autophagic marker MAP1LC3A, showed a more than 2-fold increase (Supplementary Figure S9E).

DISCUSSION

The global burden of infertility has escalated in recent years, with growing recognition of the contribution of genetic mutations to female reproductive failure. However, progress in elucidating the mechanistic underpinnings of these mutations has been hampered by the lack of suitable human-relevant animal models. This study introduces the first ZP1-deficient non-human primate model, establishing a direct link between ZP1 dysfunction and compromised oocyte structural integrity and developmental competence. Disruption of ZP1 expression led to profound architectural disorganization of the ZP and impaired folliculogenesis and oocyte maturation, underscoring its indispensable role in female fertility.

Although ZP3 has long been regarded as the principal structural component of the ZP, with heterozygous mutations leading to infertility (Chen et al., 2017), clinical evidence increasingly implicates *ZP1* mutations as a significant genetic determinant of infertility. Emerging case reports and sequencing studies over the past five years have identified recurrent *ZP1* variants in women presenting with oocyte abnormalities, ZP defects, and EFS (Luo et al., 2020; Nishimura et al., 2019; Yuan et al., 2019; Zhou et al., 2019).

Rodent models have been instrumental in providing insights into the functional genomics of reproductive biology, yet their translational relevance remains limited. In mice, only homozygous mutations in *ZP2* or *ZP3* result in infertility, while *ZP1* knockout mice remain fertile (Rankin et al., 1999). In rats, *ZP1* knockout induces infertility with complete ZP loss and aberrant oocyte morphology (Lv et al., 2021). However, sequence homology analyses reveal only 58%–68% identity between rat and human ZP proteins, indicating substantial interspecies divergence in ZP composition and function. Notably, complete *ZP4* knockout in rats has been shown to have no impact on oogenesis, ovulation, fertilization, or fertility (Zeng et al., 2021), a finding that contrasts sharply with clinical phenotypes observed in women harboring *ZP4* mutations (Wei et al., 2022; Zou et al., 2019).Compared to rodents, cynomolgus monkeys exhibit markedly higher sequence identity with humans across the ZP1–ZP4 proteins (94%, 92%, 92%, and 93%, respectively), indicating greater conservation of functional and pathogenic mechanisms. In ZP1-deficient macaques, reproductive impairments included disorganized ZP structure, disrupted follicular development, mitochondrial dysfunction, and early embryonic arrest. These abnormalities were associated with diminished oocyte competence and impaired follicular maturation, potentially driven by oxidative stress and enhanced mitochondrial autophagy. This primate model provides a powerful platform for investigating the molecular basis of ZP formation and fertilization, offering critical insights into ZP1-related infertility in humans.

TEM and immunofluorescence analyses of *ZP1*-edited oocytes revealed significant abnormalities in the outer layer of the ZP. Notably, ZP1 protein levels were markedly reduced, accompanied by a decrease in ZP3 abundance. ZP2 and ZP4 were primarily localized to the inner ZP region, with only a modest decline observed in ZP4 signal intensity. Structural integrity was compromised, evidenced by a blurred boundary between the inner and outer ZP regions and a notable decrease in electron-dense granules within the outer layer.

Previous studies have linked ZP1 deficiency in humans to complete ZP absence (Huang et al., 2014), oocyte degeneration, and EFS (Xu et al., 2020; Zou et al., 2022). Consistent with these observations, the *ZP1*-edited macaque model, characterized by multiple genotypes, recapitulated these phenotypes, as determined by H&E staining and light microscopy. Furthermore, evidence from this model suggests that *ZP1* mutations may impair the development of primordial follicles. Transcriptomic profiling revealed up-regulation of endocytosis-related pathways and concurrent down-regulation of G-protein-coupled receptor (GPCR) signaling, receptor-ligand interactions, and other granulosa-oocyte communication pathways. These findings suggest weakened regulatory crosstalk between granulosa cells and oocytes. Histological analysis further supported this hypothesis, demonstrating increased frequencies of morphologically abnormal primordial and primary follicles in *ZP1*-mutant ovaries. These findings highlight the multifaceted impact of ZP1 deficiency on ovarian follicle development, granulosa-oocyte communication, and cell cycle regulation, which collectively contribute to reproductive impairments in *ZP1*-mutant macaques.

Disruption in the ZP has been linked to failed cumulus-oocyte complex (COC) formation. *In vitro* studies have demonstrated that oocytes lacking supportive granulosa cells often undergo degeneration (Fang et al., 2024; Sun et al., 2023). The degenerative oocyte phenotypes observed in ZP1-deficient macaques—including empty zona structures, cytoplasmic degradation, and detachment from granulosa cells—resemble those described in COC formation failure. These data suggest that loss of ZP1 compromises the structural and signaling interface between granulosa cells and oocytes, contributing to degenerative outcomes. This is consistent with findings that LHCGR disruption in granulosa cells weakens intercellular communication with oocytes, promoting degeneration and EFS-like phenotypes.

Integrated transcriptomic and proteomic analyses of *ZP1*-mutant oocytes revealed coordinated dysregulation of pathways associated with mitochondrial damage, functional impairment, and autophagy. Oocytes lacking ZP1 also exhibited hallmark features of oxidative damage, including pathological mitochondrial swelling. These findings align with previous evidence linking ovarian oxidative stress to follicular depletion and diminished oocyte quality (Zhang et al., 2022), both of which are implicated in the etiology of EFS. Oxidative stress and mitochondrial dysfunction have been shown to disrupt folliculogenesis and compromise reproductive competence (Lai et al., 2023; Smits et al., 2023), reinforcing their relevance to the pathophysiological features observed in ZP1-mutant macaques. In parallel, single-oocyte RNA-seq data indicated enhanced G2/S checkpoint signaling and cell cycle dysregulation, which may account for the observed decline in oocyte maturation rates and increased proportion of blastocyst-stage cells.

Among mitochondrial antioxidant defenses, SOD2, localized to the mitochondrial membrane (Tsai et al., 2021). Its depletion has been linked to mitochondrial dysfunction, pathological hypertrophy (Peugnet et al., 2022), and autophagy (Cui et al., 2025; Iskandar et al., 2024; Nie et al., 2022). Consistent with these mechanisms, transcriptomic and proteomic datasets revealed suppressed SOD2 expression in *ZP1*-mutant oocytes. Lipid peroxidases such as ALOXE3 and ALOX12B have also been implicated in mitochondrial

dysfunction and autophagy (Li et al., 2021). Their overexpression may reflect disturbances in mitochondrial energy metabolism, resulting in excessive lipid metabolism and elevated unsaturated fatty acid production, subsequently contributing to cellular oxidative damage. Collectively, these findings underscore the complex consequences of ZP1 deficiency, including disrupted folliculogenesis, impaired granulosa cell-oocyte signaling, and dysregulation of key pathways involved in cell cycle control, oxidative stress, and mitochondrial function. Together, these factors contribute to the pronounced reproductive impairments observed in *ZP1*-mutant macaques.

Although this study successfully developed a *ZP1* gene-edited female macaque model and effectively replicated the disease phenotype associated with ZP1 deficiency in humans, several limitations should be mentioned. Due to constraints in macaque availability and reproductive capacity, only a single *ZP1*-edited female was obtained, restricting both technical and biological replication. Moreover, low blastocyst formation rates in *ZP1*-mutant oocytes impeded extensive embryo transfer experiments. A preliminary transfer of three embryos into one recipient led to early miscarriage after two months of gestation, underscoring the need for future trials involving multiple recipients and larger embryo cohorts.

Despite these limitations, this study established the first *ZP1*-knockout cynomolgus macaque model, closely recapitulating the pathological and clinical features of *ZP1*-related infertility in humans. The spatial distribution of ZP1, ZP2, ZP3, and ZP4 within the ZP was confirmed, and ZP1 deficiency was shown to disrupt follicular development and oocyte integrity. The findings further implicated oxidative stress as a key factor driving oocyte degeneration. This model provides a critical platform for studying the molecular basis of infertility and advancing diagnostic and therapeutic strategies.

DATA AVAILABILITY

Transcript and protein sequencing data were deposited in the Science Data Bank (ScienceDB) under project accession number 10.57760/sciencedb.j00139.00211, Sequence Read Archive (SRA) of the National Center for Biotechnology Information (NCBI) under BioProjectID PRJNA1273651, and Genome Sequence Archive (GSA) of the China National Center for Bioinformation (CNCB) under accession number PRJCA036317.

SUPPLEMENTARY DATA

Supplementary data to this article can be found online.

COMPETING INTERESTS

The authors declare that they have no competing interests.

AUTHORS' CONTRIBUTIONS

S.H.Y., C.H.D., and J.L.L. designed and supervised the study. W.M., B.Z.L., D.H., Y.T.F., L.L.Z., X.Y.Z., J.T.Z. and C.H.L. performed the experiments. B.Z.L., C.G.X., Y.Q.L., Y.T.Z. M.H.L., and S.K.Z. prepared the samples. W.M. performed bioinformatic analyses. S.H.Y., W.M., B.Z.L., and Y.L.G. analyzed the data and results. S.H.Y., C.H.D., J.L.L., W.M., B.Z.L., and D.H. wrote the manuscript with input from all authors. All authors read and approved the final version of the manuscript.

ACKNOWLEDGMENTS

We would like to express our thanks to Xiao-Xian Wu and Ji-Lei Huang from the Instrumental Analysis & Research Center of South China Agricultural University for their support in TEM and CLSM techniques.

REFERENCES

Abramson J, Adler J, Dunger J, et al. 2024. Accurate structure prediction of biomolecular interactions with AlphaFold 3. *Nature*, **630**(8016): 493–500.

Cao GY, Yu LN, Fang JS, et al. 2024. *ZP1*-Y262C mutation causes abnormal zona pellucida formation and female infertility in humans. *Frontiers in Genetics*, **15**: 1407202.

Chen TL, Bian YH, Liu XM, et al. 2017. A recurrent missense mutation in *ZP3* causes empty follicle syndrome and female infertility. *American Journal of Human Genetics*, **101**(3): 459–465.

Cui Y, Bai MY, Gao S, et al. 2025. Zinc ions facilitate metabolic bioenergetic recovery post spinal cord injury by activating microglial mitophagy through the STAT3-FOXO3a-SOD2 pathway. *Free Radical Biology and Medicine*, **227**: 64–79.

Dai C, Chen YZ, Hu L, et al. 2019. *ZP1* mutations are associated with empty follicle syndrome: evidence for the existence of an intact oocyte and a zona pellucida in follicles up to the early antral stage. A case report. *Human Reproduction*, **34**(11): 2201–2207.

El-Mestrah M, Castle PE, Borossa G, et al. 2002. Subcellular distribution of ZP1, ZP2, and ZP3 glycoproteins during folliculogenesis and demonstration of their topographical disposition within the zona matrix of mouse ovarian oocytes. *Biology of Reproduction*, **66**(4): 866–876.

Epifano O, Liang LF, Familari M, et al. 1995. Coordinate expression of the three zona pellucida genes during mouse oogenesis. *Development*, **121**(7): 1947–1956.

Familiari G, Relucenti M, Heyn R, et al. 2006. Three-dimensional structure of the zona pellucida at ovulation. *Microscopy Research and Technique*, **69**(6): 415–426.

Fang JS, Sun H, Chen LJ, et al. 2024. Embryological characteristics and clinical outcomes of oocytes with different degrees of abnormal zona pellucida during assisted reproductive treatment. *Zygote*, **32**(1): 7–13.

Hou MQ, Zhu LX, Jiang JH, et al. 2022. Novel heterozygous mutations in *ZP2* cause abnormal zona pellucida and female infertility. *Reproductive Sciences*, **29**(10): 3047–3054.

Huang HL, Lv C, Zhao YC, et al. 2014. Mutant ZP1 in familial infertility. *New England Journal of Medicine*, **370**(13): 1220–1226.

Iskandar K, Foo J, Liew AQX, et al. 2024. A novel MTORC2–AKT–ROS axis triggers mitofission and mitophagy-associated execution of colorectal cancer cells upon drug-induced activation of mutant KRAS. *Autophagy*, **20**(6): 1418–1441.

Jimenez-Movilla M, Dean J. 2011. ZP2 and ZP3 cytoplasmic tails prevent premature interactions and ensure incorporation into the zona pellucida. *Journal of Cell Science*, **124**(6): 940–950.

Kim D, Pertea G, Trapnell C, et al. 2013. TopHat2: accurate alignment of transcriptomes in the presence of insertions, deletions and gene fusions. *Genome Biology*, **14**(4): R36.

Lai XL, Xiong WJ, Li LS, et al. 2023. Zinc deficiency compromises the maturational competence of porcine oocyte by inducing mitophagy and apoptosis. *Ecotoxicology and Environmental Safety*, **252**: 114593.

Lefièvre L, Conner SJ, Salpekar A, et al. 2004. Four zona pellucida glycoproteins are expressed in the human. *Human Reproduction*, **19**(7): 1580–1586.

Li CF, Zhang Y, Liu J, et al. 2021. Mitochondrial DNA stress triggers autophagy-dependent ferroptotic death. *Autophagy*, **17**(4): 948–960.

Liao Y, Smyth GK, Shi W. 2014. featureCounts: an efficient general purpose program for assigning sequence reads to genomic features. *Bioinformatics*, **30**(7): 923–930.

Liberzon A, Birger C, Thorvaldsdóttir H, et al. 2015. The molecular signatures database hallmark gene set collection. *Cell Systems*, **1**(6): 417–425.

Liu SL, Zuo HY, Zhao BW, et al. 2023. A heterozygous *ZP2* mutation causes zona pellucida defects and female infertility in mouse and human.

iScience, **26**(10): 107828.

Liu WQ, Li KM, Bai DD, et al. 2017. Dosage effects of ZP2 and ZP3 heterozygous mutations cause human infertility. *Human Genetics*, **136**(8): 975–985.

Love MI, Huber W, Anders S. 2014. Moderated estimation of fold change and dispersion for RNA-seq data with DESeq2. *Genome Biology*, **15**(12): 550.

Luo G, Zhu LX, Liu ZX, et al. 2020. Novel mutations in *ZP1* and *ZP2* cause primary infertility due to empty follicle syndrome and abnormal zona pellucida. *Journal of Assisted Reproduction and Genetics*, **37**(11): 2853–2860.

Lv C, Huang HL, Yi DJ, et al. 2021. Mutant *Zp1* impedes incorporation of ZP3 and ZP4 in the zona pellucida, resulting in zona absence and female infertility in rats. *Biology of Reproduction*, **104**(6): 1262–1270.

Ma YH, Li JY, Wang G, et al. 2016. Efficient production of cynomolgus monkeys with a toolbox of enhanced assisted reproductive technologies. *Scientific Reports*, **6**: 25888.

Männikkö M, Törmälä RM, Tuuri T, et al. 2005. Association between sequence variations in genes encoding human zona pellucida glycoproteins and fertilization failure in IVF. *Human Reproduction*, **20**(6): 1578–1585.

Matzuk MM, Burns KH, Viveiros MM, et al. 2002. Intercellular communication in the mammalian ovary: oocytes carry the conversation. *Science*, **296**(5576): 2178–2180.

Moros-Nicolás C, Chevret P, Jiménez-Movilla M, et al. 2021. New insights into the mammalian egg zona pellucida. *International Journal of Molecular Sciences*, **22**(6): 3276.

Müller T, Kalxdorf M, Longuespée R, et al. 2020. Automated sample preparation with SP3 for low-input clinical proteomics. *Molecular Systems Biology*, **16**(1): e9111.

Nie S, Shi Z, Shi MY, et al. 2022. PPARγ/SOD2 protects against mitochondrial ROS-dependent apoptosis via inhibiting ATG4D-mediated mitophagy to promote pancreatic cancer proliferation. *Frontiers in Cell and Developmental Biology*, **9**: 745554.

Nishimura K, Dioguardi E, Nishio S, et al. 2019. Molecular basis of egg coat cross-linking sheds light on ZP1-associated female infertility. *Nature Communications*, **10**(1): 3086.

Peugnet V, Chwastyniak M, Mulder P, et al. 2022. Mitochondrial-targeted therapies require mitophagy to prevent oxidative stress induced by SOD2 inactivation in hypertrophied cardiomyocytes. *Antioxidants*, **11**(4): 723.

Phillips DM, Shalgi RM. 1980. Surface properties of the zona pellucida. *Journal of Experimental Zoology*, **213**(1): 1–8.

Picelli S, Faridani OR, Björklund ÅK, et al. 2014. Full-length RNA-seq from single cells using Smart-seq2. *Nature Protocols*, **9**(1): 171–181.

Rankin T, Talbot P, Lee E, et al. 1999. Abnormal zonae pellucidae in mice lacking ZP1 result in early embryonic loss. *Development*, **126**(17): 3847–3855.

Smits MAJ, Schomakers BV, van Weeghel M, et al. 2023. Human ovarian aging is characterized by oxidative damage and mitochondrial dysfunction. *Human Reproduction*, **38**(11): 2208–2220.

Sun L, Fang X, Chen ZH, et al. 2019. Compound heterozygous *ZP1* mutations cause empty follicle syndrome in infertile sisters. *Human Mutation*, **40**(11): 2001–2006.

Sun LW, Tong KY, Liu WW, et al. 2023. Novel variants in *ZP1, ZP2* and *ZP3* associated with empty follicle syndrome and abnormal zona pellucida. *Reproductive BioMedicine Online*, **46**(5): 847–855.

Tsai YT, Yeh HY, Chao CT, et al. 2021. Superoxide dismutase 2 (SOD2) in vascular calcification: a focus on vascular smooth muscle cells, calcification pathogenesis, and therapeutic strategies. *Oxidative Medicine and Cellular Longevity*, **2021**: 6675548.

Wassarman PM, Litscher ES. 2021. Zona pellucida genes and proteins: essential players in mammalian oogenesis and fertility. *Genes*, **12**(8): 1266.

Wei XL, Li YZ, Liu QC, et al. 2022. Mutations in *ZP4* are associated with abnormal zona pellucida and female infertility. *Journal of Clinical Pathology*, **75**(3): 201–204.

Wu TZ, Hu EQ, Xu SB, et al. 2021. clusterProfiler 4.0: a universal enrichment tool for interpreting omics data. *The Innovation*, **2**(3): 100141.

Xu QH, Zhu XL, Maqsood M, et al. 2020. A novel homozygous nonsense ZP1 variant causes human female infertility associated with empty follicle syndrome (EFS). *Molecular Genetics & Genomic Medicine*, **8**(7): e1269.

Xue ZG, Huang K, Cai CC, et al. 2013. Genetic programs in human and mouse early embryos revealed by single-cell RNA sequencing. *Nature*, **500**(7464): 593–597.

Yuan P, Li RQ, Li D, et al. 2019. Novel mutation in the *ZP1* gene and clinical implications. *Journal of Assisted Reproduction and Genetics*, **36**(4): 741–747.

Zeng MH, Wang Y, Huang HL, et al. 2021. *Zp4* is completely dispensable for fertility in female rats. *Biology of Reproduction*, **104**(6): 1282–1291.

Zhang BB, Qu GG, Nan YC, et al. 2022. Ovarian oxidative stress induced follicle depletion after zona pellucida 3 vaccination is associated with subfertility in BALB/c mice. *Frontiers in Veterinary Science*, **9**: 814827.

Zhang DZ, Zhu LX, Liu ZX, et al. 2021. A novel mutation in *ZP3* causes empty follicle syndrome and abnormal zona pellucida formation. *Journal of Assisted Reproduction and Genetics*, **38**(1): 251–259.

Zhang WH, Aida T, del Rosario RCH, et al. 2020. Multiplex precise base editing in cynomolgus monkeys. *Nature Communications*, **11**(1): 2325.

Zhang Y, Skolnick J. 2005. TM-align: a protein structure alignment algorithm based on the TM-score. *Nucleic Acids Research*, **33**(7): 2302–2309.

Zhang Z, Shangguan T, Li YY, et al. 2018. Infertility due to lack of zona pellucida caused by a compound heterozygous mutation in *ZP1* gene. *Reproductive and Developmental Medicine*, **2**(3): 183–186.

Zhou Z, Ni CX, Wu L, et al. 2019. Novel mutations in *ZP1, ZP2*, and *ZP3* cause female infertility due to abnormal zona pellucida formation. *Human Genetics*, **138**(4): 327–337.

Zhu AQ, Ibrahim JG, Love MI. 2019. Heavy-tailed prior distributions for sequence count data: removing the noise and preserving large differences. *Bioinformatics*, **35**(12): 2084–2092.

Zou TT, Xi QS, Liu ZX, et al. 2022. A novel homozygous nonsense mutation in *ZP1* causes female infertility due to empty follicle syndrome. *Reproductive Sciences*, **29**(12): 3516–3520.

Zou Y, Zhou JY, Guo JB, et al. 2019. Mutation analysis of ZP1, ZP2, ZP3 and ZP4 genes in 152 Han Chinese samples with ovarian endometriosis. *Mutation Research/Fundamental and Molecular Mechanisms of Mutagenesis*, **813**: 46–50.